ACS OMEGA

http://pubs.acs.org/journal/acsodf

Article

Correlation between the Intrinsic Photophysical Properties of the Spirobifluorene-Derived Monomer

Jie Wang and Dong Shi*

Cite This: *ACS Omega* 2021, 6, 5972−5980

Read Online

ACCESS | Metrics & More | Article Recommendations | Supporting Information

ABSTRACT: Spiro-molecules derived from the functional spirobifluorene core play important roles in the frontiers of diverse optoelectronics. The optoelectronics of these molecules have been intensively studied without yielding a knowledge base of precisely parameterized photophysical properties. Here, we report the precisely parameterized photophysics of spiro-OMeTAD, one prototypical optoelectronic spirobifluorene derivative. The use of a preobtained single-crystalline pure spiro-OMeTAD solid for the solution preparation allows for accurate determination of its molar absorption coefficient (ε) in its monomer form. A near-unity photoluminescence quantum yield ($\Phi_L \sim 99\%$) was observed from the monomer solution. The monomer's photoluminescence decay follows a mono-exponential channel that results in a lifetime (τ) of $\sim$ 1.64 ns. Taken together ε, Φ_L, and τ correlate well via the Strickler−Berg equation. The Strickler−Berg relationship among the key photophysical properties determined on spiro-OMeTAD applies for spirobifluorene derivatives, as verified in an extended test on the newly created spiro-mF. Practical issues that may lead to misparameterized photophysical properties of these molecules are emphasized. Our results of the precisely parameterized photophysical properties of the spiro-OMeTAD monomer in dilute solution serve as background references for studying the optoelectronic processes in the technically more useful thin-film form in practical optoelectronic devices.

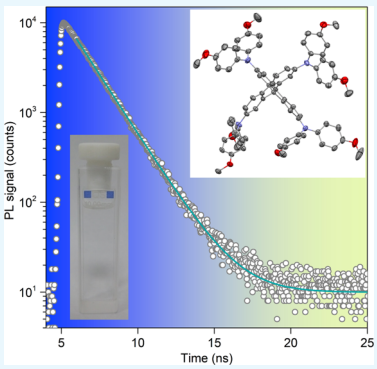

INTRODUCTION

Spiro-linkage as a useful molecular designing strategy has played a substantial role in the rapid progress of the emerging organic electronics and solution-processed optoelectronics.[1−9] In the past two decades, a large number of spiro-compounds with advanced electronic and optoelectronic functionalities have been created using this strategy. In particular, two functional molecular fragments are linked in a perpendicular arrangement via a spiro-carbon atom that adopts an sp^3 hybridized configuration. This allows for remarkably improved solution processability and morphological tunability, while the optical and electronic properties of each individual molecular moiety are retained.[3,6]

The basic optoelectronic functionality of spiro-compounds is directly linked to the spiro-core. In particular, a spirobifluorene core is a prototypical structure based on which a wide array of spiro-molecules have been created for diverse optoelectronic applications. While some of the spirobifluorene derivatives have shown long-standing dominance in the emerging solution-processed photovoltaics, new alternatives are being created as well; for example, the long-standing spiro-OMeTAD [2,2′,7,7′-tetrakis(*N*,*N*-di-*p*-methoxyphenyl-amine)9,9′-spirobifluorene] and the newly demonstrated spiro-mF (see Figure 1a,b) in solution-processed perovskite solar cells (PSCs).[3,4] Remarkably, the use of hole-conducting spiro-OMeTAD as a solid-state replacement to liquid electrolytes led to significantly improved device stability for both dye-sensitized solar cells (DSSCs) and PSCs.[4,7,8] By the time of writing, the solar-to-electric power conversion efficiency (PCE) of PSCs have already excelled among other solution-processed solar technologies within a remarkably short timeframe based on the solid-state strategy.[10,11]

At present, the use of spiro-OMeTAD molecules continues to set new benchmarks for PSCs.[12−15] Recent studies indicate that enhancing the intermolecular ordering within the solid thin-film layer could lead to further improved hole-conducting performance,[16,17] pushing the mechanistic studies on the optoelectronic process within spiro-OMeTAD to the center of intense focus.[18−21] However, precisely parameterized photophysical properties of spiro-OMeTAD in its monomer form remains an outstanding quest. This hinders improved understanding on the optoelectronics of this novel molecular hole conductor and further structural tailoring toward improved performances.[19,22−26] The problems lie in the natural tendency of incorporating small solvent molecules into the solids of spiro-molecules. This may lead to inaccurate determination of the exact molar amount of the sample and eventually inaccurate calculation of the molar absorption coefficient (ε).

Received: January 14, 2021
Accepted: February 11, 2021
Published: February 18, 2021

https://dx.doi.org/10.1021/acsomega.1c00262
ACS Omega 2021, 6, 5972−5980

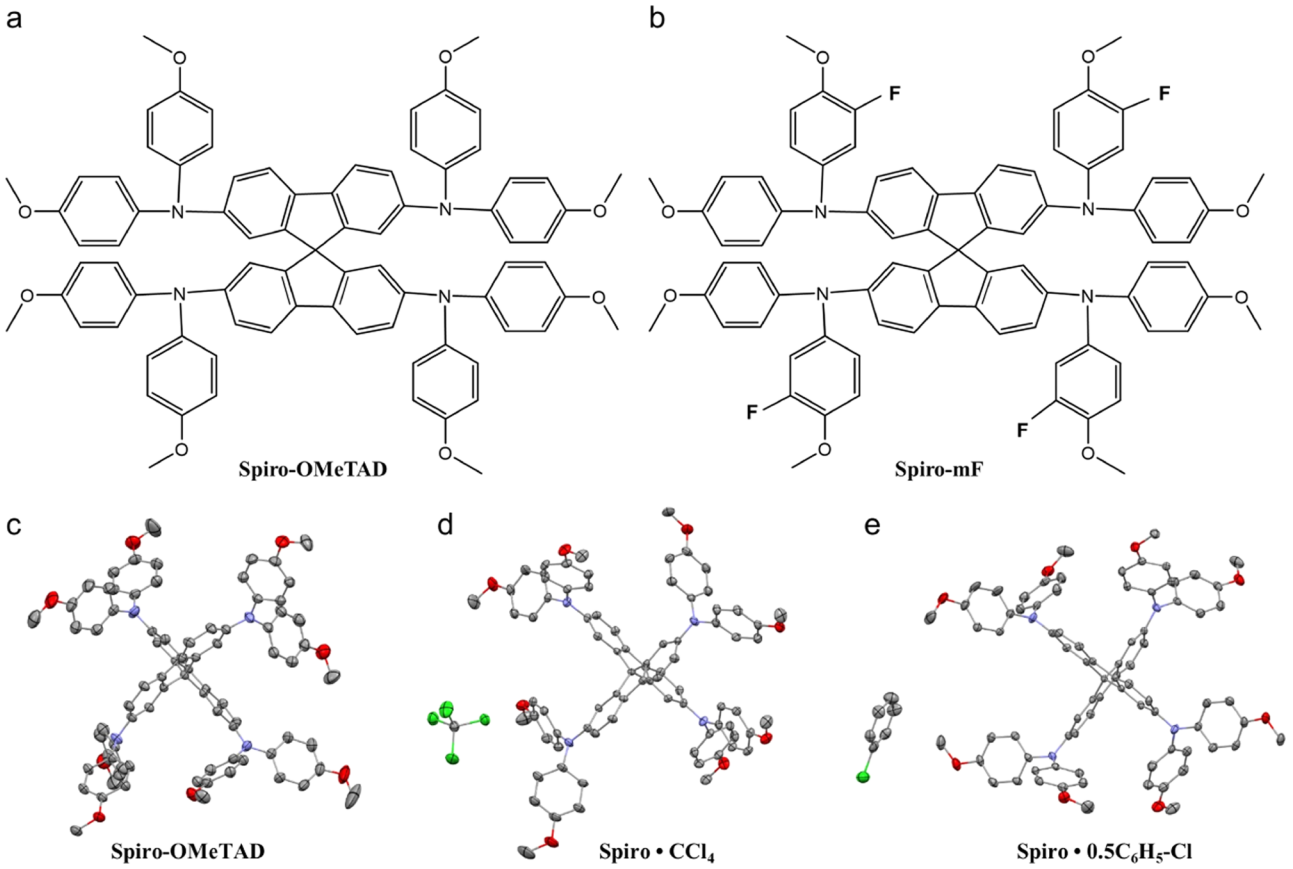

Figure 1. Molecular structures and single-crystal X-ray diffraction (SC-XRD) results. (a, b) Molecular structures of spiro-OMeTAD and spiro-mF, (c–e) single-crystal structure of the spiro-OMeTAD monomer, spiro-OMeTAD·CCl_4, and spiro-OMeTAD·0.5C_6H_5-Cl; thermal ellipsoids are at the 30% probability level. Hydrogen atoms are omitted for clarity. C: gray; N: blue; O: red; and Cl: green.

In fact, disparities beyond instrumental errors have been witnessed from the reported ε values of spiro-OMeTAD in its monomer form in dilute solution.[9,27]

We, therefore, sought to acquire a solid knowledge base about the key photophysical properties of the spiro-OMeTAD monomer by avoiding the aforementioned problem of incorporation. In other words, single-crystalline pure spiro-OMeTAD solids without incorporating any molecules are required. Fortunately, a recently reported antisolvent vapor-assisted crystallization (AVC) method allows obtaining single-crystalline pure spiro-OMeTAD solids.[16] In particular, the use of dimethyl sulfoxide (DMSO) with a relatively larger molecular size instead of the normally used chlorobenzene was suggested to avoid solvent incorporation during crystallization.

RESULTS AND DISCUSSION

Single crystals of pure spiro-OMeTAD were obtained via the AVC method,[16] with the experimental details given in the Experimental Section. Figure 1c shows the crystal structure of pure spiro-OMeTAD without incorporating any solvent molecules. Notably, the spiro-OMeTAD molecule is characterized by a rigid three-dimensional (3D) configuration with the two MeOTAD chains connected perpendicularly via the central spiro-carbon atom. The perpendicular spiro-linkage of the two long chains creates large hollow spaces at the peripheries of the spiro-entirety, allowing for the incorporation of small solvent molecules therein.

Cocrystallization of spiro-molecules with small solvent molecules, particularly those used for dissolving them and controllable solution-base thin-film formation, has been well demonstrated in previous studies.[16,27] To further verify the natural tendency of cocrystallization between the studied spiro-OMeTAD molecules and small solvent molecules, we tested the cocrystallization between spiro-OMeTAD and CCl_4, since the cocrystallization between spiro-OMeTAD and C_6H_5-Cl has already been reported eleswhere.[9] Note that CCl_4 is a nonpolar solvent whose molecular structure is completely free of π-electrons.

Analogously to the aforementioned crystallization of pure spiro-OMeTAD, the AVC method was used. In brief, spiro-OMeTAD was dissolved in CCl_4 in a vial that was then placed inside a larger vial that contained the antisolvent, CH_3OH, in which spiro-OMeTAD does not dissolve. The antisolvent was allowed to slowly evaporate into the inner vial, which eventually caused the solution in the inner vial to become supersaturated so that not all of the spiro-OMeTAD could be dissolved. Subsequently, part of the spiro-OMeTAD crystallized out of the solution phase in the form of needle-like single crystals. The as-obtained single crystals were characterized by single-crystal X-ray diffraction (SC-XRD), resulting in the single-crystal structure of spiro-OMeTAD·CCl_4, as given in Figure 1d.

We then replaced CCl_4 with C_6H_5-Cl for a parallel test and obtained needle-like spiro-OMeTAD·0.5C_6H_5-Cl single crystals (Figure 1e). Remarkably, the half-molar incorporation of C_6H_5-Cl into spiro-OMeTAD solids when crystallized out of

https://dx.doi.org/10.1021/acsomega.1c00262
ACS Omega 2021, 6, 5972–5980

the solution phase was in exact agreement with the previous report.[9] Thus, the natural tendency of cocrystallization of small solvent molecules with spiro-OMeTAD is unambiguously confirmed. This should be taken into account when weighing the as-received spiro-OMeTAD solid samples for molar amount calculation and subsequent quantification of photophysical properties like the molar absorption coefficient.

We then moved on to the optical characterizations of spiro-OMeTAD in its monomer form in dilute solution. The use of the preobtained single-crystalline pure spiro-OMeTAD without any solvent molecules for solution preparation allows for accurate determination of the solution's molar concentration. To keep our study in line with the predominant research thrust, we used chlorobenzene as the solvent. Note that chlorobenzene has been the only widely used solvent for dissolving spiro-OMeTAD and subsequent layer formation for diverse studies.

The ultraviolet−visible (UV−vis) absorption spectrum of spiro-OMeTAD in chlorobenzene exhibits a predominant absorption band that peaks at 390 nm, as shown in Figure 2a,

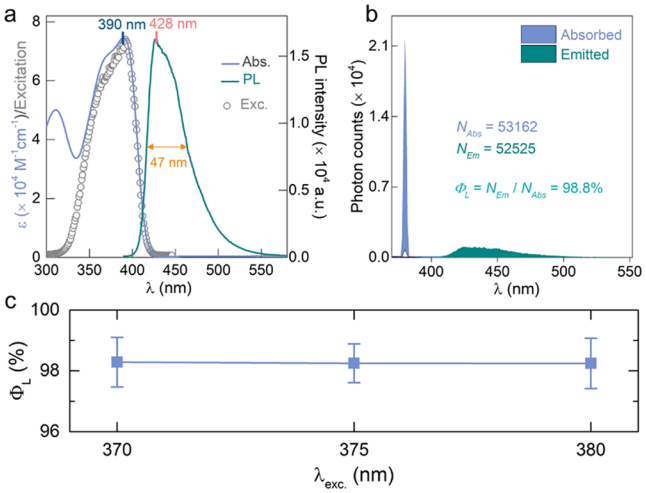

Figure 2. Spectroscopic results of the spiro-OMeTAD dilute solution in chlorobenzene. (a) Absorption (left, solid line), photoluminescence (PL) (right, solid line), and excitation (left, open circles) spectra. (b) Time-correlated single-photon counting (TCSPC) data collected the absolute PL quantum yield (PLQY) measurement. (c) PLQY (average value from five parallel tests) as a function of the excitation wavelength.

left. In addition, a shoulder around 370 nm is observed, consistent with previous observations.[23,28,29] The occurrence of the shoulder structure indicates energy level splitting between the two spiro-linked OMeTAD chains, as elaborated by the aid of density functional theory (DFT) calculations.[17] ε_{max} (at 390 nm) was determined to be 7.5×10^4 M^{-1} cm^{-1}, slightly larger than the frequently reported values ~6.9×10^4 M^{-1} cm^{-1}.[23]

The dilute solution spiro-OMeTAD monomer in chlorobenzene exhibits strong photoluminescence (PL) and the spectrum is displayed in Figure 2a, right. Notably, the PL peak appears at 428 nm and carries a shoulder at ~448 nm. At first sight, the PL spectra lineshape mirrors the first band absorption well, while the full spectral mirror-image relationship is observed between the PL and the excitation traces (gray circles in Figure 2a). The mirror-image relationship between the first band absorption and emission is characteristic of monomer emission. In addition, recording the PL generated at different photoexcitation wavelengths results in identical PL (Figure S1, Supporting Information). Such invariant nature of PL against varied excitation energies rules out hot excited state emission, leaving behind the emission that solely occurs from the thermalized first excited state. On the other hand, the observed Stokes shift of 38 nm of spiro-OMeTAD is only about a half of that characterized by the single-chain organic chromophores that are structurally similar to MeOTAD,[28,29] which is due to the enhanced structural rigidity upon spiro-linkage. The structural rigidity guarantees a minor nuclear displacement associated with the electronic transition between its ground and excited states.

We also evaluated the emissivity of the spiro-OMeTAD monomer in chlorobenzene by measuring its absolute PL quantum yield (PLQY) with an integrating sphere. Practically, both the absorbed and the emitted photons were precisely counted by the equipped time-correlated single-photon counting (TCSPC) detector. Then, the PLQY is calculated according to $\Phi_L = N_{Em}/N_{Abs}$.[30] In this expression, Φ_L is the absolute PLQY value, $N_{Em}$is the number of photons emitted, and N_{Abs} is the number of photons absorbed. The validity of the integrating sphere and TCSPC detector was verified with rhodamine 6G, a PLQY standard that is characterized by a known Φ_L of 94% in dilute ethanol solution (Figures S2 and S3, Supporting Information).[30,31]

Figure 2b shows the TCSPC data collected in the absolute PLQY measurement. Note that the excitation wavelength was set at 380 nm to avoid any energy overlap between the absorbed and emitted photons. N_{Abs}, N_{Em}, and Φ_L are also reported in Figure 2b. The near-unity PLQY (Φ_L = 98.8%) rules out interchain electronic coupling between the two perpendicularly oriented MeOTAD fragments, torsional vibrations, chemical defects along the chains, or impurities as potential channels that may deactivate the excited state. We also monitored its PLQY at two higher excitation energies at 375 and 370 nm, demonstrating the invariant Φ_L value as a function of photoexcitation energy (Figure 2c). The TCSPC data of the PLQY monitored at 370 and 375 nm excitation are provided in Figure S4a,b in the Supporting Information.

We then proceeded to evaluate the PL-lifetime of the spiro-OMeTAD monomer in its dilute solution by time-resolved PL (TRPL) measurements. A picosecond pulsed laser exciting at 400 nm was used as the photoexcitation source. TRPL traces monitored at 415, 428, 445, 460, 475, and 490 nm are shown in Figure 3a. Notably, all of the TRPL traces decay over three decades without much deviation following a pure single-exponential function.

Figure 3b shows the analyzed details of the TRPL trace (blue markers) monitored at the PL peak at 428 nm. A single-exponential fit (green solid line) based on the nonlinear least-squares (NLLS) analysis is plotted along with the traces. A reduced chi square is also reported, demonstrating that the single-exponential function fits the TRPL trace quite well. In addition, the standard deviation, δ_k, one more parameter that evaluates the goodness-of-fit (GOF) is also provided, as shown in Figure 3c. The overall central symmetric distribution of δ_k around the zero-line also indicates high-level GOF. A general introduction to the NLLS analysis based on exponential models and the rational evaluation of the GOF are provided in the Supporting Information. TRPL traces (Figure 3a) monitored at other wavelengths are also analyzed and the results are given in Figure S5a−e in the Supporting

https://dx.doi.org/10.1021/acsomega.1c00262
ACS Omega 2021, 6, 5972−5980

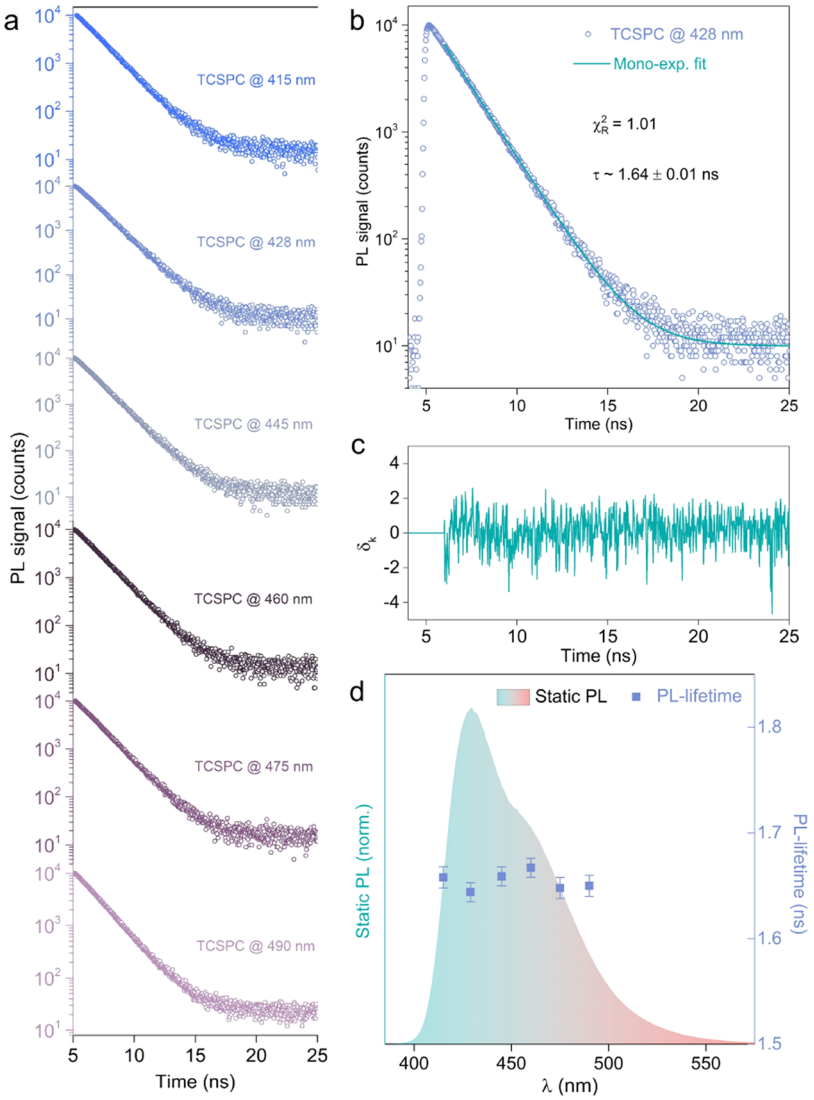

Figure 3. TRPL results of the spiro-OMeTAD dilute solution in chlorobenzene. (a) TRPL traces monitored at 415, 428, 445, 460, 475, and 490 nm. (b) TRPL trace (open circles) monitored at the PL peak at 428 nm along with a single-exponential fit (solid line). (c) Standard deviation associated with a single-exponential fit to the TRPL trace monitored at 428 nm. (d) PL-lifetimes (right, solid squares) against the monitored PL-wavelengths plotted along with the normalized static PL (left). The error bar only reflects the fitting uncertainty.

Information. As expected, an invariant PL-lifetime of, $\tau \sim 1.64$ ns, was determined from all cases. PL-lifetimes obtained by fitting the TRPL traces monitored at different PL-wavelengths are marked along with the static-PL plot, as shown in Figure 3d.

Taken together, the PLQY and the PL-lifetime, the radiative rate constant k_r is calculated to be 6.03×10^8 s^{-1} according to $k_r = \Phi_L/\tau$. Here, it is worthy to remark that the rigid structure of the spiro-OMeTAD monomer represents an ideal model as assumed by Strickler and Berg in dealing with the inherent relationship between the absorption intensity and the PL-lifetimes of single molecules.[32] The Strickler–Berg relation holds across a wide variety of monomer compounds including complex coordinated molecule structures.[33,34] According to the Strickler–Berg equation, the radiative rate constant k_r^0 can be calculated according to $k_r^0 = (2.88 \times 10^{-9}\ ms^{-1})v^2n^2A$. In our case, A denotes the integration of the extinction coefficient intensity between 22 000 cm^{-1} and 27 000 cm^{-1}, which corresponds to the first absorption band of the spiro-OMeTAD monomer. n denotes the refractive index of the solution. Since the concentration of spiro-OMeTAD in chlorobenzene is sufficiently low, the refractive index of chlorobenzene, $n = 1.525$, is used instead, and v denotes the PL wave number.

The calculated A, k_r^0, and τ_0 (natural lifetime) are summarized in Table 1, together with the experimentally determined natural PL-lifetime, τ. Note that for single-exponential PL-decaying molecules, $\tau_0 = \tau/\Phi_L$ and is reciprocal to the k_r^0. Good agreement between the experimentally determined k_r value and the calculated k_r^0 is confirmed, which indicates that the precisely parameterized photophysical properties of spiro-OMeTAD monomers are accurately correlated via the Strickler–Berg relationship.

We further found that the Strickler–Berg relationship between the key photophysical properties as verified from the spiro-OMeTAD monomer also applies for other spirobifluorene derivatives, e.g., spiro-mF. The molecular structure of spiro-mF is given in Figure 1b. Spiro-mF is a newly created spirobifluorene derivative that has recently led to benchmark efficiency for PSCs.[3] The photophysical results of

https://dx.doi.org/10.1021/acsomega.1c00262
ACS Omega 2021, 6, 5972−5980

Table 1. Photophysical Parameters of Spiro-OMeTAD and Spiro-mF Dilute Solution in Chlorobenzene

sample	spiro-OMeTAD	spiro-mF
λ_{max}^{Abs} (nm)	390	388
λ_{max}^{PL} (nm)	428	421
ε_{max} (M^{-1} cm^{-1})	7.45×10^4	8.22×10^4
FWHM (nm)	47	58
τ (ns)	1.64	1.47
Φ_L	98.8%	99%
k_r^0 (s^{-1})	6.27×10^8	6.8×10^8
$\tau_0{}^a$ (ns)	1.59	1.47
$\tau_0{}^b$ (ns)	1.66	1.48

[a]Calculated data. [b]Experimental data.

the spiro-mF monomer in dilute solution of chlorobenzene are grouped in Figure 4. In particular, Figure 4a shows the static absorption, PL, and excitation spectra of spiro-mF in chlorobenzene. Notably, spiro-mF exhibits an absorption onset around 430 nm, which is basically the same as that observed for spiro-OMeTAD (Figure 2a). However, the peak position of its first band absorption is blue-shifted by 2 nm with respect to spiro-OMeTAD, which is most likely due to the introduction of electronically more negative fluorine elements. The PL spectrum of spiro-mF is a bit wider than that of spiro-OMeTAD. The full widths at half-maximum (FWHM) exhibited by the PL of both spiro-mF and spiro-OMeTAD are summarized in Table 1, together with the other important photophysical parameters. The PL-lifetime of ~1.47 ns was obtained from the TRPL results of spiro-mF (Figure 4b). The absolute PLQY measurements resulted in a Φ_L value of ~99% for spiro-mF (Figure 4c). Summarized together, the Strickler–Berg relationship applies for both spiro-OMeTAD and spiro-mF (Table 1). Very likely, the Strickler–Berg relationship may well apply for the whole family of spirobifluorene derivatives.

The precisely parameterized photophysical properties (absorption coefficient, PL-lifetime, and PLQY) of spiro-OMeTAD monomers and their inherent correlations via the Strickler–Berg relationship can be referred as the background knowledge. Based on this, the consequent spectral changes in their thin-film form can be better understood and implicated. Technically, the solid thin-film form of the functional spirobifluorene derivatives is more important for practical optoelectronic applications. In this regard, we also characterized the photophysical properties of spiro-OMeTAD in the thin-film form. Practically, the spiro-OMeTAD thin-film is prepared precisely according to the fully matured procedures developed along with solution-processed solar cell fabrication. In general, the prepared amorphous thin film is boundary-free (Figure S6, Supporting Information) and uniform in thickness ~184 nm (Figure S7, Supporting Information). The normally used salt additives are avoided, thereby ruling out any extrinsic effects on the photophysical responses.

Figure 5a shows the static absorbance and front-face PL of the amorphous spiro-OMeTAD thin film. Characters of random aggregates shown by the broad structureless first absorption band as well as the long tail that extends far toward long wavelengths are demonstrated (Figure 5a, left). In contrast, the PL spectrum of the amorphous spiro-OMeTAD thin film exhibits the basic character of monomer emission without any fingerprints of aggregate emissions (Figure 5a, right). In fact, a better-resolved shoulder structure characteristic of spiro-OMeTAD monomer emission is observed from the solid thin film. This is probably due to the reduced freedom of each individual spiro-OMeTAD molecule in the solid thin films compared to the free mobile monomer in the dilute solution.

Although the PL from the thin film also emanates predominantly from monomer emission, the absolute PLQY is significantly decreased. As measured, the absolute PLQY of spiro-OMeTAD thin films is typically below 10%. Figure 5b shows the typical absolute PLQY result of the thin films. The much lower PLQY indicates nonradiative deactivation of the excited state that occurs in a much faster way in the solid thin films. Since the thin film is free of additive impurities, the nonradiative excited state deactivation can only occur in an intermolecular way, which may account for intermolecular charge hopping, with much advantage to its hole-conducting functionality in the thin-film form as used in practical optoelectronic devices.

We also checked the PL-lifetime of the spiro-OMeTAD thin film (Figure 5c). It was found that the TRPL traces (gray makers in Figure 5c) of the thin film could not be as well fitted using one single-exponential function as in the monomer case. The mono-exponential fit (solid blue line in Figure 5c) leads to a poor reduced chi square value of 4.321, as shown in Figure 5d, together with the large standard deviations. Biexponential functions fit the TRPL trace better, yielding an improved reduced chi square value of 1.366, as shown in Figure 5e, together with the standard deviation. The bi-exponential fitting plot, the green dashed line, is also shown along with the TRPL traces in Figure 5b. The two lifetime components obtained from the biexponential fit are also shown in Figure 5b. As expected, two much shorter lifetime components with τ_1 of ~

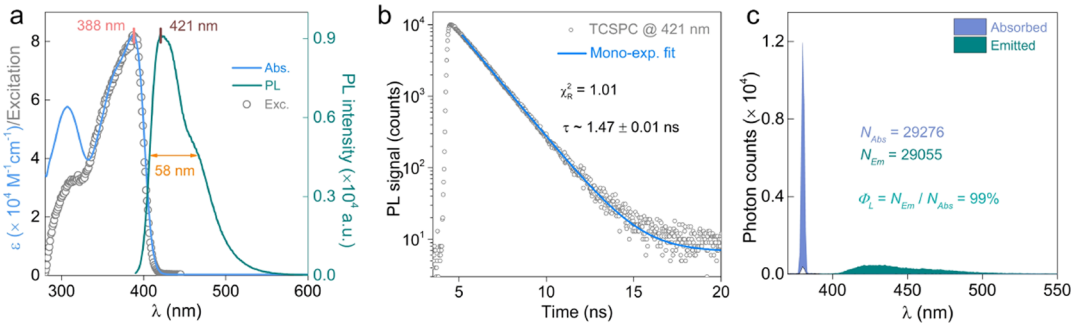

Figure 4. Spectroscopic results of the spiro-mF dilute solution in chlorobenzene. (a) Absorption (left, solid line), PL (right, solid line), and excitation (left, open circles) spectra. (b) TRPL traces (gray markers) monitored at 421 nm along with the mono-exponential fit (blue solid line). (c) TCSPC data collected from the absolute PLQY measurement.

https://dx.doi.org/10.1021/acsomega.1c00262
ACS Omega 2021, 6, 5972−5980

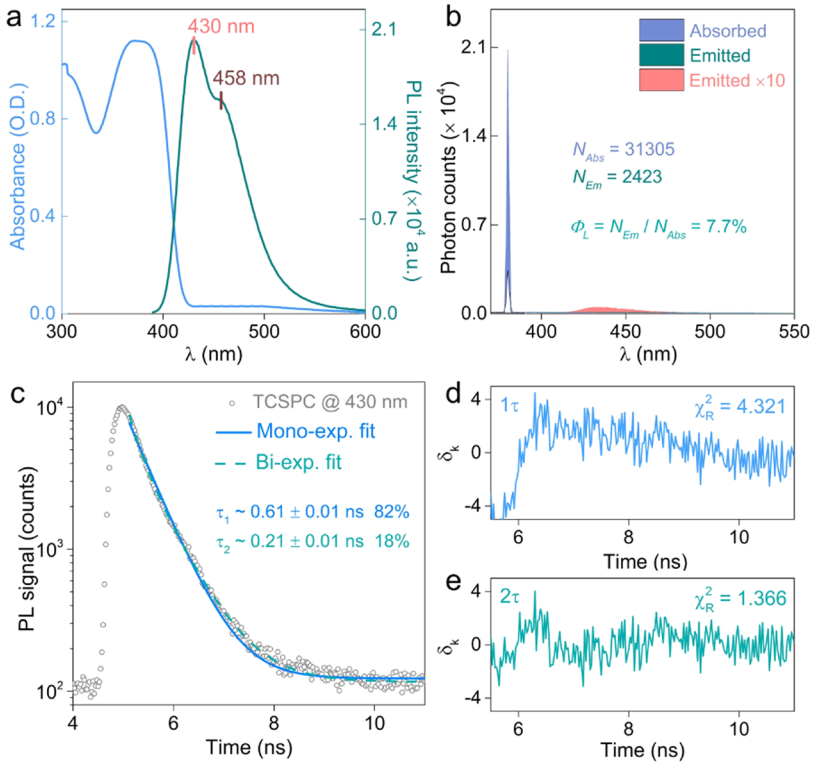

Figure 5. Spectroscopic results of amorphous spiro-OMeTAD thin films. (a) Absorbance (left) and PL (right) spectra. (b) TCSPC data collected from the absolute PLQY measurement. (c) TRPL traces (open circles) monitored at 430 nm along with mono- (solid line) and biexponential (dashed line) fits. (d) and (e) Standard deviations associated with the mono- and biexponential fit. Reduced chi squares are also reported, demonstrating that the biexponential fit performs better than the mono-exponential one.

0.61 ns and τ_2 ~ 0.21 ns are determined, indicating much faster deactivation of the excited carriers in the thin-film form. More in-depth studies are required to fully understand the electronic transporting mechanism in the solid thin films of spiro-OMeTAD and other functional spirobifluorene derivatives.

CONCLUSIONS

In summary, using preobtained single-crystalline pure spiro-OMeTAD without incorporating any solvent molecules for solution preparation, we precisely parameterized the basic photophysical properties of spiro-OMeTAD in its monomer form in dilute solution. We found that the precise parameterized molar absorption coefficient, PL-lifetime, and the absolute PLQY of spiro-OMeTAD monomers correlate well via the Strickler−Berg equation. Thus, quantified correlationship applies well for other spirobifluorene derivatives and probably the whole family of spirobifluorene derivatives. Our characterization is largely standardized and the results of the precisely paramaterized photophysical properties of the long-standing hole conductor spiro-OMeTAD can serve as a background reference knowledge for further in-depth mechanistic studies on their optoelectronic functionalities.

EXPERIMENTAL SECTION

Materials. Spiro-OMeTAD (purity ≥ 99.5%, product no. PLT502011T) and spiro-mF (product no. PLT502191T) were purchased from Xi'an Polymer Light Technology Corp. Chlorobenzene (sublimated purity, product no. 01007005), CCl_4 (product no. 01162305), DMSO (product no. 01104495), methanol (product no. 01104357), ethanol (product no. 01376276), and rhodamine 6G (product no. 01474150) were purchased from Shanghai Titan Technology Co., Ltd. All reagents were used as-received.

Solution Preparation. Spiro-OMeTAD (0.2 mg) and spiro-mF (0.2 mg) were fully dissolved in chlorobenzene under stirring, yielding 10 mL of clear solution in a volumetric flask. Then, the clear solution was transferred into scrupulously clean quartz cuvettes for spectroscopic characterizations. For crystallization, the solution was prepared by dissolving 20 mg of spiro-OMeTAD, respectively, in DMSO (4 mL), CCl_4 (4 mL), and chlorobenzene (4 mL). After stirring at room temperature for 4 h in a closed vial in the dark, the solution was filtered through a syringe filter (Ø = 0.22 μm) prior to placing into an outer larger vial that was filled with the antisolvent. The standard rhodamine 6G solution in ethanol was of 0.002 mg/mL concentration for PLQY verifications.

Crystal Growth. Antisolvent vapor-assisted crystallization (AVC), which has been proved to be effective for growing high-quality spiro-OMeTAD single crystals, has been used to grow high-quality single crystals of both the spiro-OMeTAD monomer and its mixed form cocrystallized with the solvent molecules, as discussed in this study. In particular, the filtered solution (~4 mL) of spiro-OMeTAD in CCl_4 (5 mg/mL) was equally divided into four vials (5 mL), and then was placed inside a big vial (10 mL) containing methanol (~5 mL). The outer vial was closed tightly and transferred into a nitrogen-filled glovebox. Once transferred, the crystallization systems were covered in the dark and kept stable at room temperature. Slow evaporation of the antisolvent, methanol, into the solution of spiro-OMeTAD triggered the crystallization of spiro-OMeTAD·CCl_4 at room temperature. Single crystals of spiro-OMeTAD and spiro-OMeTAD·0.5C_6H_5-Cl were ob-

https://dx.doi.org/10.1021/acsomega.1c00262
ACS Omega 2021, 6, 5972−5980

tained using the same procedures, simply by changing to the right solution in the inner vials.

Thin-Film Fabrication. The amorphous spiro-OMeTAD thin film was prepared in full accordance to the fully matured spin-coating method, which is widely used in practical solar cell device fabrication. In particular, 72 mg of spiro-OMeTAD was dissolved in chlorobenzene (1 mL), forming a clear solution that was then subjected to prolonged stirring for 4 h at room temperature. The solution was filtered through a syringe filter (Ø = 0.22 μm) prior spin coating onto the precleaned 1 × 1 cm^2 quartz substrates. The substrates were washed in an ultrasonic cleaner with an abstergent, deionized water, acetone, and isopropanol, with each step taking 15 min. Once cleaning was done, the wet substrates were dried with a nitrogen gas gun and put into a plasma cleaning machine to fully remove any potential organic residues. Spiro-OMeTAD thin films were coated on the quartz substrate by spinning (3000 rpm, 30 s), and eventually dried under vacuum at 60°C for 4 h.

Atomic Force Microscopy (AFM). The surface topography and height profile of the spiro-OMeTAD film sample were characterized by Asylum MFP-3D atomic force microscopy (AFM). A scalpel was applied to make two scratches on the surface of the freshly prepared film for height measurement. AC mode was used for the surface imaging scanning, with the driving frequency set near the preoptimized resonance frequency for all of the following morphological imaging. With the probe scanning back and forth on the sample surface, the surface morphology was recorded by a piezoelectric sensor and displayed for analysis.

Single-Crystal X-ray Diffraction (SC-XRD). A colorless single-crystal specimen with a long sheet-like shape was scooped into a microloop and mounted on a Bruker D8 Venture for SC-XRD characterization. The diffractometer is equipped with a Iμs 3.0 X-ray source (Mo Kα, λ = 0.71073 Å) and Photon II detector. Combined φ and ω scans allow us to minimize the data collection time, while retaining the maximized resolution and multiplicity of observations. The X-ray diffraction data were collected under ambient laboratory conditions, and the crystal structure was solved and refined using the Bruker SHELXTL software package. Detailed crystal structure information is summarized in Table S1 in the Supporting Information.

Elemental Analysis. The bulk purity and stoichiometry of the as-grown single crystals were checked by elemental analysis. Calcd for spiro-OMeTAD: C, 79.39; H, 5.59; N, 4.57. Found: C, 78.97; H, 5.68; N, 4.62. Calcd for spiro-mF: C, 74.99; H, 4.97; N, 4.32. Found: C, 74.75; H, 4.92; N, 4.36. Calcd for spiro-OMeTAD·CCl_4: C, 71.41; H, 4.97; N, 4.06. Found: C, 71.35; H, 4.99; N, 4.04. Calcd for spiro-OMeTAD·0.5C_6H_5-Cl: C, 78.72; H, 5.54; N, 4.37. Found: C, 78.68; H, 5.57; N, 4.39.

UV−Vis Absorption. The absorbance of spiro-OMeTAD and spiro-mF solutions was recorded in a transmission mode using a Shimadzu UV-2600 spectrometer. The colorless solvent chlorobenzene was checked prior to testing the solutions, showing no reference absorption in the characterization range between 300 and 600 nm.

Steady-State Photoluminescence (PL). The steady-state PL was recorded using a FluoTime 300 fluorometer (PicoQuant) equipped with two light sources. A 300 W coaxial xenon arc lamp with a parabolic reflector was used as the excitation light source. Setting the PL detection range between 390 and 600 nm while verifying the excitation wavelength yields duplicate spectra in their normalized form.

Excitation Spectrum. The excitation spectrum of the spiro-OMeTAD and spiro-mF solutions was recorded with a xenon lamp on FluoTime 300, with the monitoring emission fixed at 460 nm. In addition, we also monitored the excitation spectra at 465 and 470 nm, which yielded identically the same result as the case for 460 nm.

Photoluminescence Quantum Yield (PLQY). The absolute PLQY measurements of the spiro-OMeTAD solution, spiro-mF solution, and rhodamine 6G solution were performed on a FluoTime 300 spectrometer equipped with an integrating sphere. In particular, a xenon lamp was used as the excitation light source, exciting the spiro-OMeTAD and spiro-mF solution samples at 380 nm. Pure chlorobenzene solvent was used as the blank reference. The absorbed photons were numbered in the range between 370 and 390 nm, while the emitted photons were numbered between 390 and 600 nm, as shown in Figure 2b in the main text as displayed in different colors. Then, the absolute PLQY of the spiro-OMeTAD solution was equated by dividing the total number of emitted photons by the total number of absorbed photons. In parallel, the absolute PLQY value obtained in this way for rhodamine 6G was 94.2%, in strict agreement with the known standard value, thereby validating our PLQY measurements.

Time-Resolved Photoluminescence (TRPL). TRPL characterizations were also performed on the FluoTime 300 spectrometer equipped with a time-correlated single-photon counting (TCSPC) detector. The pulsed LDH 405 laser diode (λ = 400 nm) with a repetition rate set at 32 MHz was used as the excitation source. The TRPL traces were spectrally resolved using a single-grating spectrometer and acquired using a time-correlated detector operated in single-photon counting mode. All of the TRPL traces of the spiro-OMeTAD samples probed at different positions were recorded with the same repetition rate, laser intensity, and pulse width.

■ ASSOCIATED CONTENT

Supporting Information

The Supporting Information is available free of charge at https://pubs.acs.org/doi/10.1021/acsomega.1c00262.

Brief introduction to nonlinear least square analysis; excitation wavelength-dependent photoluminescence spectra; spectra of the PLQY standard rhodamine 6G; PLQY measurement details; fitting details of PL-decay; AFM images of thin-film samples; and single-crystal data (PDF)

Spiro-OMeTAD (CIF)

Spiro-CCl4 (CIF)

Spiro-0.5CB (CIF)

■ AUTHOR INFORMATION

Corresponding Author

Dong Shi − *School of Optoelectronic Science and Engineering, University of Electronic Science and Technology of China, Chengdu 610054, P. R. China;* orcid.org/0000-0003-2128-3698; Email: dshi@uestc.edu.cn

Author

Jie Wang − *School of Optoelectronic Science and Engineering, University of Electronic Science and Technology of China, Chengdu 610054, P. R. China*

https://dx.doi.org/10.1021/acsomega.1c00262
ACS Omega 2021, 6, 5972−5980

Complete contact information is available at:
https://pubs.acs.org/10.1021/acsomega.1c00262

Author Contributions

D.S. conceived and directed this research. J.W. performed the experiments. J.W. and D.S. analyzed the data. J.W. processed the figures and prepared the Supporting Information. D.S. wrote the manuscript.

Notes

The authors declare no competing financial interest.

■ ACKNOWLEDGMENTS

Part of this work was supported by the National Natural Science Foundation of China under Grant No. 51872038. D.S. acknowledges the financial support from UESTC.

■ REFERENCES

(1) Farazdel, A.; Dupuis, M.; Clementi, E.; Aviram, A. Electric field induced intramolecular electron transfer in spiro-electron systems and their suitability as molecular electronic devices. A theoretical study. *J. Am. Chem. Soc.* **1990**, *112*, 4206−4214.

(2) Salbeck, J.; Yu, N.; Bauer, J.; Weissortel, F.; Bestgen, H. Low molecular organic glasses for blue electroluminescence. *Synth. Met.* **1997**, *91*, 209−215.

(3) Jeong, M.; Choi, I. W.; Go, E. M.; Cho, Y.; Kim, M.; Lee, B.; Jeong, S.; Jo, Y.; Choi, H. W.; Lee, J.; Bae, J.-H.; Kwak, S. K.; Kim, D. S.; Yang, C. Stable perovskite solar cells with efficiency exceeding 24.8% and 0.3-V voltage loss. *Science* **2020**, *369*, 1615−1620.

(4) Bach, U.; Lupo, D.; Comte, P.; Moser, J. E.; Weissortel, F.; Salbeck, J.; Spreitzer, H.; Grätzel, M. Solid-state dye-sensitized mesoporous TiO_2 solar cells with high photon-to-electron conversion efficiencies. *Nature* **1998**, *395*, 583−585.

(5) Frank, S.; Jörg, S.; Matthias, S.; Jürgen, S.; Albrecht, W.; Hubert, S.; Frank, W.; Josef, S. White light emission from organic LEDs utilizing spiro compounds with high temperature stability. *Adv. Mater.* **2000**, *12*, 130−133.

(6) Saragi, T. P.; Spehr, T.; Siebert, A.; Fuhrmann-Lieker, T.; Salbeck, J. Spiro compounds for organic optoelectronics. *Chem. Rev.* **2007**, *107*, 1011−1065.

(7) Kim, H. S.; Lee, C. R.; Im, J. H.; Lee, K. B.; Moehl, T.; Marchioro, A.; Moon, S. J.; Humphry-Baker, R.; Yum, J. H.; Moser, J. E.; Grätzel, M.; Park, N. G. Lead iodide perovskite sensitized all-solid-state submicron thin film mesoscopic solar cell with efficiency exceeding 9%. *Sci. Rep.* **2012**, *2*, No. 591.

(8) Lee, M. M.; Teuscher, J.; Miyasaka, T.; Murakami, T. N.; Snaith, H. J. Efficient hybrid solar cells based on meso-superstructured organometal halide perovskites. *Science* **2012**, *338*, 643−647.

(9) Ganesan, P.; Fu, K.; Gao, P.; Raabe, I.; Schenk, K.; Scopelliti, R.; Luo, J.; Wong, L. H.; Grätzel, M.; Nazeeruddin, M. K. A simple spiro-type hole transporting material for efficient perovskite solar cells. *Energy Environ. Sci.* **2015**, *8*, 1986−1991.

(10) Lin, Y.-H.; Sakai, N.; Da, P.; Wu, J.; Sansom, H. C.; Ramadan, A. J.; Mahesh, S.; Liu, J.; Oliver, R. D. J.; Lim, J.; Aspitarte, L.; Sharma, K.; Madhu, P. K.; Morales-Vilches, A. B.; Nayak, P. K.; Bai, S.; Gao, F.; Grovenor, C. R. M.; Johnston, M. B.; Labram, J. G.; Durrant, J. R.; Ball, J. M.; Wenger, B.; Stannowski, B.; Snaith, H. J. A piperidinium salt stabilizes efficient metal-halide perovskite solar cells. *Science* **2020**, *369*, 96−102.

(11) Lu, H.; Liu, Y.; Ahlawat, P.; Mishra, A.; Tress, W. R.; Eickemeyer, F. T.; Yang, Y.; Fu, F.; Wang, Z.; Avalos, C. E.; Carlsen, B. I.; Agarwalla, A.; Zhang, X.; Li, X.; Zhan, Y.; Zakeeruddin, S. M.; Emsley, L.; Rothlisberger, U.; Zheng, L.; Hagfeldt, A.; Gratzel, M. Vapor-assisted deposition of highly efficient, stable black-phase $FAPbI_3$ perovskite solar cells. *Science* **2020**, *370*, No. eabb8985.

(12) McMeekin, D. P.; Sadoughi, G.; Rehman, W.; Eperon, G. E.; Saliba, M.; Horantner, M. T.; Haghighirad, A.; Sakai, N.; Korte, L.; Rech, B.; Johnston, M. B.; Herz, L. M.; Snaith, H. J. A mixed-cation lead mixed-halide perovskite absorber for tandem solar cells. *Science* **2016**, *351*, 151−155.

(13) Saliba, M.; Matsui, T.; Domanski, K.; Seo, J. Y.; Ummadisingu, A.; Zakeeruddin, S. M.; Correa-Baena, J. P.; Tress, W. R.; Abate, A.; Hagfeldt, A.; Grätzel, M. Incorporation of rubidium cations into perovskite solar cells improves photovoltaic performance. *Science* **2016**, *354*, 206−209.

(14) Tan, H.; Jain, A.; Voznyy, O.; Lan, X.; Arquer, F. P. G.; Fan, J. Z. R.; Bermudez, Q.; Yuan, M.; Zhang, B.; Zhao, Y.; Fan, F.; Li, P.; Quan, L. N.; Zhao, Y. Z.; Lu, H.; Yang, Z.; Hoogland, S.; Sargent, E. H. Efficient and stable solution-processed planar perovskite solar cells via contact passivation. *Science* **2017**, *355*, 722−726.

(15) Wang, R.; Xue, J.; Wang, K. L.; Wang, Z. K.; Luo, Y.; Fenning, D.; Xu, G.; Nuryyeva, S.; Huang, T.; Zhao, Y.; Yang, J. L.; Zhu, J.; Wang, M.; Tan, S.; Yavuz, I.; Houk, K. N.; Yang, Y. Constructive molecular configurations for surface-defect passivation of perovskite photovoltaics. *Science* **2019**, *366*, 1509−1513.

(16) Shi, D.; Adinolfi, V.; Comin, R.; Yuan, M.; Alarousu, E.; Buin, A.; Chen, Y.; Hoogland, S.; Rothenberger, A.; Katsiev, K.; Losovyj, Y.; Zhang, X.; Dowben, P. A.; Mohammed, O. F.; Sargent, E. H.; Bakr, O. M. Low trap-state density and long carrier diffusion in organolead trihalide perovskite single crystals. *Science* **2015**, *347*, 519−522.

(17) Li, Y.; Li, H.; Zhong, C.; Sini, G.; Brédas, J.-L. Characterization of intrinsic hole transport in single-crystal spiro-OMeTAD. *npj Flex. Electron.* **2017**, No. 2.

(18) Hawash, Z.; Ono, L. K.; Qi, Y. Moisture and oxygen enhance conductivity of LiTFSI-doped spiro-MeOTAD hole transport layer in perovskite solar cells. *Adv. Mater. Inter.* **2016**, *3*, No. e1600117.

(19) Brauer, J. C.; Lee, Y. H.; Nazeeruddin, M. K.; Banerji, N. Ultrafast charge carrier dynamics in $CH_3NH_3PbI_3$: evidence for hot hole injection into spiro-OMeTAD. *J. Mater. Chem. C* **2016**, *4*, 5922−5931.

(20) Namatame, M.; Yabusaki, M.; Watanabe, T.; Ogomi, Y.; Hayase, S.; Marumoto, K. Direct observation of dramatically enhanced hole formation in a perovskite-solar-cell material spiro-OMeTAD by Li-TFSI doping. *Appl. Phys. Lett.* **2017**, *110*, No. 123904.

(21) Forward, R. L.; Chen, K. Y.; Weekes, D. M.; Dvorak, D. J.; Cao, Y.; Berlinguette, C. P. Protocol for quantifying the doping of organic hole-transport materials. *ACS Energy Lett.* **2019**, *4*, 2547−2551.

(22) Cappel, U. B.; Daeneke, T.; Bach, U. Oxygen-induced doping of spiro-MeOTAD in solid-state dye-sensitized solar cells and its impact on device performance. *Nano Lett.* **2012**, *12*, 4925−4931.

(23) Malinauskas, T.; Saliba, M.; Matsui, T.; Daskeviciene, M.; Urnikaite, S.; Gratia, P.; Send, R.; Wonneberger, H.; Bruder, I.; Grätzel, M.; Getautis, V.; Nazeeruddin, M. K. Branched methoxydiphenylamine-substituted fluorene derivatives as hole transporting materials for high-performance perovskite solar cells. *Energy Environ. Sci.* **2016**, *9*, 1681−1686.

(24) Schölin, R.; Karlsson, M. H.; Eriksson, S. K.; Siegbahn, H.; Johansson, E. M. J.; Rensmo, H. Energy level shifts in spiro-OMeTAD molecular thin films when adding Li-TFSI. *J. Phys. Chem. C* **2012**, *116*, 26300−26305.

(25) Burschka, J.; Kessler, F.; Nazeeruddin, M. K.; Grätzel, M. Co(III) complexes as p-dopants in solid-state dye-sensitized solar cells. *Chem. Mater.* **2013**, *25*, 2986−2990.

(26) Zhang, W.; Wang, L.; Guo, Y.; Zhang, B.; Leandri, V.; Xu, B.; Li, Z.; Gardner, J. M.; Sun, L.; Kloo, L. Single crystal structure and opto-electronic properties of oxidized spiro-OMeTAD. *Chem. Commun.* **2020**, *56*, 1589−1592.

(27) Guo, A.; Zhu, R. 2,2′,7,7′-Tetra-bromo-9,9′-spiro-bifluorene toluene hemisolvate. *Acta Crystallogr., Sect. E: Crystallogr. Commun.* **2009**, *65*, No. o1528.

(28) Li, H.; Fu, K.; Hagfeldt, A.; Grätzel, M.; Mhaisalkar, S. G.; Grimsdale, A. C. Angew. A simple 3,4-Ethylenedioxythiophene based hole-transporting material for perovskite solar cells. *Angew. Chem.* **2014**, *53*, 4085−4088.

(29) Wang, H.; Sheikh, A. D.; Feng, Q.; Li, F.; Chen, Y.; Yu, W.; Alarousu, E.; Ma, C.; Haque, M. A.; Shi, D.; Wang, Z. S.; Mohammed,

https://dx.doi.org/10.1021/acsomega.1c00262
ACS Omega 2021, 6, 5972−5980

O. F.; Bakr, O. M.; Wu, T. Facile synthesis and high performance of a new carbazole-based hole-transporting material for hybrid perovskite solar cells. *ACS Photonics* **2015**, *2*, 849−855.
(30) Lakowicz, J. R. *Principles of Fluorescence Spectroscopy*; Springer: New York, 2006; pp 27−60.
(31) Fischer, M.; Georges, J. Fluorescence quantum yield of rhodamine 6G in ethanol as a function of concentration using thermal lens spectrometry. *Chem. Phys. Lett.* **1996**, *260*, 115−118.
(32) Strickler, S. J.; Berg, R. A. Relationship between absorption intensity and fluorescence lifetime of molecules. *J. Chem. Phys.* **1962**, *37*, 814−822.
(33) Chábera, P.; Liu, Y.; Prakash, O.; Thyrhaug, E.; Nahhas, A. E.; Honarfar, A.; Essen, S.; Fredin, L. A.; Harlang, T. C.; Kjaer, K. S.; Handrup, K.; Ericson, F.; Tatsuno, H.; Morgan, K.; Schnadt, J.; Haggstrom, L.; Ericsson, T.; Sobkowiak, A.; Lidin, S.; Huang, P.; Styring, S.; Uhlig, J.; Bendix, J.; Lomoth, R.; Sundstrom, V.; Persson, P.; Warnmark, K. A low-spin Fe(iii) complex with 100-ps ligand-to-metal charge transfer photoluminescence. *Nature* **2017**, *543*, 695−699.
(34) Kjær, K. S.; Kaul, N.; Prakash, O.; Chabera, P.; Rosemann, N. W.; Honarfar, A.; Gordivska, O.; Fredin, L. A.; Bergquist, K. E.; Haggstrom, L.; Ericsson, T.; Lindh, L.; Yartsev, A.; Styring, S.; Huang, P.; Uhlig, J.; Bendix, J.; Strand, D.; Sundstrom, V.; Persson, P.; Lomoth, R.; Warnmark, K. Luminescence and reactivity of a charge-transfer excited iron complex with nanosecond lifetime. *Science* **2019**, *363*, 249−253.

https://dx.doi.org/10.1021/acsomega.1c00262
ACS Omega 2021, 6, 5972−5980